Mon. Not. R. Astron. Soc. **000**, 000–000 (2001)

Gravitational lensing: effects of cosmology and of lens and source profiles

F. Perrotta[1,2], C. Baccigalupi[2], M. Bartelmann[3], G. De Zotti[1], G. L. Granato[1]

[1] *Oss. Astr. Padova, Vicolo dell'Osservatorio 5, I-35122 Padova, Italy. Email:* perrotta@sissa.it, dezotti@pd.astro.it, granato@pd.astro.it

[2] *SISSA/ISAS, Astrophysics Sector, Via Beirut, 4, I-34014 Trieste, Italy. Email:* bacci@sissa.it

[3] *Max-Planck Institut für Astrophysik, P.O. Box 1317, D–85741 Garching, Germany. Email:* msb@mpa-garching.mpg.de

1 February 2001

ABSTRACT

We present detailed calculations of the magnification distribution, including both weak and strong lensing, using very recent solutions of the Dyer-Roeder (1973) equation for light propagation in a inhomogeneous universe with a cosmological constant and up-to-date models for the evolving cosmological distribution of dark matter halos. We address in particular the effect on the magnification distribution of a non-zero cosmological constant, of different density profiles of lenses, and of finite sizes of lensed sources, three important issues not yet fully settled.
We show that, if dark matter fluctuations are normalized to the local cluster abundance, in the presence of a cosmological constant the optical depth for lensing *decreases* compared to the case of an Einstein-de Sitter universe, because halos in the relevant mass range are less abundant over a large redshift interval. We also discuss the differences in the magnification probability distributions produced by Navarro, Frenk & White (NFW) and by Singular Isothermal Sphere (SIS) density profiles of lenses. We find that the NFW lens is more efficient for moderate magnifications ($2 \lesssim A \lesssim 4$), and less efficient for larger magnifications. Moreover, we discuss quantitatively the maximum magnification, $A_{\rm max}$, that can be achieved in the case of extended sources (galaxies) with realistic luminosity profiles, taking into account the possible ellipticity of the lens potential. We find that plausible values of $A_{\rm max}$ are in the range 10–30.
Finally, we apply our results to a class of sources following the luminosity evolution typical for a unified scheme of QSO formation. We find that the lensed source counts at 850 μm can be larger than the unlensed ones by several orders of magnitude at flux densities 100 mJy.

1 INTRODUCTION

Gravitational lensing is well known to be a powerful tool to probe the overall geometry of the universe at $z \lesssim 6$ and the values of cosmological parameters (curvature, vacuum energy density described either by a cosmological constant or by a dynamical quantity like quintessence, Hubble constant: Bartelmann et al. 1997; Falco et al. 1998; Cooray 1999; Huterer & Cooray 1999; Macias-Perez et al. 2000; Bhatia 2000; Helbig 2000), the evolution of large scale structure (Rix et al. 1994; Mao & Kochanek 1994; Bacon et al. 2000), the masses and the density profiles of dark halos of galaxies and galaxy clusters (Narayan 1998 and references therein; Mellier 1999; Clowe et al. 2000).

Another important effect of gravitational lensing is the modification of the observed luminosity functions of distant sources and of their counts, due to the redshift dependent magnification bias (Peacock 1982; Narayan 1989; Schneider 1992).

In view of all the above applications, it is essential to perform the most accurate modeling of all the ingredients entering into the gravitational lensing process. Quantitative predictions depend on the lens population as a function of mass and redshift, on the lens profiles, on the the luminosity function and size of the sources, and on a correct treatment of the distance-redshift relations, taking into account the effect of density inhomogeneities on the propagation of light rays.

Gravitational lensing by intervening mass concentrations is a statistical process. It can be described by a probability distribution $F(A, z_{\rm s})$ of the magnification factor A, which obviously depends on the source redshift $z_{\rm s}$. It is generally difficult to model $F(A, z_{\rm s})$ in detail analytically. Some authors estimated it with N-body simulations (see e.g. Rauch 1991; Pei 1993a,b). Nonetheless, the main features of $F(A, z_{\rm s})$ can be captured using generic properties of gravitational lensing. Strong lensing occurs near caustic curves, which cause $F(A, z_{\rm s})$ to decrease $\propto A^{-3}$ for $A \gg 1$, irrespective of the lens model (Peacock 1982; Turner et al. 1984).

In this paper we present detailed calculations of the magnification distribution, including both weak and strong lensing, using very recent solutions of the Dyer-Roeder (1973) equation for light propagation in a inhomogeneous universe with a cosmological constant (Demianski et al. 2000) to compute the relationships between distances and redshift as well as up-to-date models for the evolving cosmological distribution of dark matter halos (Sheth & Tormen 1999; Sheth et al. 1999) that can act as lenses. We address in particular the effect on the magnification distribution of a non-zero cosmological constant, of different density profiles of lenses, of a finite size and of luminosity profiles of lensed sources, three im-

portant issues not yet fully settled. The magnification probability distribution has been applied to the counts at $850\mu m$: the luminosity function of the source population used here has been inferred by the evolution of the QSOs luminosity function and from the link between the QSOs and the hosting spheroids (Granato et al. 2000). Such luminosity function turns out to fit the SCUBA data.

The plan of this paper is as follows. In Sect. 2 and 3, we describe our assumptions on the distribution of lenses in mass and redshift, and on their density profiles, respectively. In Sect. 4, we review the basic definitions of distance and flux magnification in inhomogeneous universes. In Sect. 5, we introduce the probability for a source at given redshift to be magnified by a certain amount, and quantify the magnification bias on source counts, for which a model is described in Sect. 6. In Sect. 7 we face the problem of determining the maximum magnification allowed for extended sources. We summarize and discuss our results in Sect. 8.

Throughout this paper, $\Omega_{0\mathrm{m}}$ and $\Omega_{0\Lambda}$ denote the present-day density parameters for the non-relativistic matter and for the cosmological components, respectively, neglecting the radiation energy density. The Hubble constant is $H_0 = 100\,h\,\mathrm{km\,s^{-1}\,Mpc^{-1}}$, $\Omega_{0R} \equiv 1-\Omega_{0\mathrm{m}}-\Omega_{0\Lambda}$ is the curvature term, and Ω denotes the total density parameter. Our fiducial model has $\Omega_{0\mathrm{m}}=0.3$, $\Omega_{0\Lambda}=0.7$ and $h=0.65$. Furthermore, $q_0 = -\ddot{a}a/\dot{a}^2$ is the deceleration parameter, and we concentrate on spatially-flat models ($\Omega_{0R}=0$).

2 THE EVOLVING HALO MASS FUNCTION

We assume that the lens population consists of collapsed dark matter halos with an epoch-dependent mass function described by the Sheth & Tormen (1999) function, which reproduces fairly accurately the results of extensive numerical simulations over more than four orders of magnitude in mass, for a wide range of Cold Dark Matter cosmologies (Jenkins et al. 2000). This function improves considerably on the familiar Press-Schechter (1974) model which overestimates the abundance of "typical" ($M_\star$) halos and underestimates that of massive systems. The comoving number density of halos with mass M at redshift z is then

$$\frac{\mathrm{d}n}{\mathrm{d}M} = \sqrt{\frac{2aA^2}{\pi}}\,\frac{\rho_0}{M^2}\,\frac{\delta_\mathrm{c}(z)}{\sigma(M)}\left[1+\left(\frac{\sigma(M)}{\sqrt{a}\delta_\mathrm{c}(z)}\right)^{2p}\right] \times \left|\frac{\mathrm{d}\ln\sigma}{\mathrm{d}\ln M}\right| \exp\left(-\frac{a\delta_\mathrm{c}^2(z)}{2\sigma(M)^2}\right)\,; \quad (1)$$

The best-fit values of the parameters are $a=0.707$, $p=0.3$, and $A\simeq 0.3222$ (Sheth & Tormen 1999; Sheth, Mo & Tormen 1999). The Press-Schechter mass function is recovered for $a=1$, $p=0$ and $A=0.5$.

In Eq. (1), ρ_0 is the mean mass density at a reference epoch t_0, which we assume to be the present time, and σ^2 is the variance of linear density fluctuations at the present epoch smoothed with a spherical top-hat filter $W_R(k)$ enclosing a mass M. The variance σ^2 is related to the power spectrum $P(k)$ by:

$$\sigma^2(R) = \frac{4\pi}{(2\pi)^3}\int_0^\infty \mathrm{d}k\,k^2\,W_R^2(k)\,P(k)\,, \quad (2)$$

with

$$W_R(k) = \frac{3}{(kR)^3}\left[\sin(kR)-(kR)\cos(kR)\right]. \quad (3)$$

A useful expression for $\sigma(M)$ and its derivative $\mathrm{d}\sigma/\mathrm{d}M$ was obtained by Kitayama & Suto (1996),

$$\sigma \propto (1+2.208m^d-0.7668m^{2d}+0.7949m^{3d})^{-2/(9d)}\,, \quad (4)$$

$\Gamma = \Omega_{0m}h\exp[-\Omega_{0b}(1+\sqrt{2h}/\Omega_{0m})]$ being the shape parameter (Bardeen et al. 1986) and we have adopted a present baryon density $\Omega_{0b}h^2=0.03$. For a ΛCDM model with $\Omega_{0\Lambda}=0.7$ and $\Omega_{0\mathrm{m}}=0.3$, the COBE normalization is $\sigma_8=\sigma(R=8\,h^{-1}\,\mathrm{Mpc})=0.925$ (Bunn & White 1997).

Also in Eq. (1), $\delta_\mathrm{c}^2(z)$ is the linear density contrast of an object virializing at z, evaluated at the present epoch. It can be estimated using the spherical collapse model (e.g. Peebles 1980; Lahav et al. 1991; Lacey & Cole 1993; Nakamura 1996; Eke, Cole & Frenk 1996; Łokas & Hoffman 2000) yielding:

$$\delta_\mathrm{c}(z) = \frac{\delta_\mathrm{c}\,D_+(z=0)}{D_+(z)}\,, \quad (5)$$

where $D_+(z)$ is the linear growth factor of density fluctuations:

$$D_+(z) \simeq (1+z)^{-1}\,\frac{5}{2}\,\Omega_\mathrm{m} \times [\Omega_\mathrm{m}^{4/7}-\Omega_\Lambda+(1+\Omega_\mathrm{m}/2)(1+\Omega_\Lambda/70)]^{-1}\,, \quad (6)$$

in the approximation by Carroll et al. (1992), where $\Omega_\mathrm{m}=\Omega_{0\mathrm{m}}(1+z)^3/E^2(z)$, $\Omega_\Lambda=\Omega_{0\Lambda}/E^2(z)$, and

$$E(z)=H(z)/H_0=[\Omega_{0\mathrm{m}}(1+z)^3+\Omega_{0R}\,(1+z)^2+\Omega_{0\Lambda}]^{1/2}\,. \quad (7)$$

δ_c [Eq. (5)] is the value of the critical overdensity evaluated at virialization. An approximate expression valid for any cosmological model was reported by Nakamura (1996) and Kitayama & Suto (1996):

$$\delta_\mathrm{c} \approx \frac{3(12\pi)^{2/3}}{20}\,(1+0.0123\log_{10}\Omega_\mathrm{m})\,. \quad (8)$$

3 GRAVITATIONAL LENSING AND HALO MODELS

The ray-tracing equation relates the position of a source to the impact parameter in the lens plane of a light ray connecting source and observer. The light ray passing the lens at an impact parameter $\vec{\zeta}$ is bent by an angle $\hat{\alpha}(\vec{\zeta})$. The source position $\vec{\eta}$ and the impact parameter $\vec{\zeta}$ in the lens plane are related through

$$\vec{\eta} = \frac{D_\mathrm{s}}{D_\mathrm{d}}\,\vec{\zeta} - D_\mathrm{ds}\,\vec{\hat{\alpha}}(\vec{\zeta})\,, \quad (9)$$

where $D_\mathrm{d,s,ds}$ are the angular-diameter distances between observer and lens, observer and source, and lens and source, respectively. We will specify these distances later in the context of a "clumpy universe". The deflection angle $\vec{\hat{\alpha}}$ is the sum of the deflections due to all mass elements of the lens projected on the lens plane,

$$\vec{\hat{\alpha}}(\vec{\zeta}) = \frac{4G}{c^2}\int_{R^2}\frac{\vec{\zeta}-\vec{\zeta}'}{\left|\vec{\zeta}-\vec{\zeta}'\right|^2}\,\Sigma(\vec{\zeta}')\,\mathrm{d}^2\zeta'\,, \quad (10)$$

where Σ is the surface mass density of the lens.

It is convenient to introduce the dimensionless impact parameter $\vec{x}=\vec{\zeta}/\zeta_0$, where ζ_0 is an arbitrary length scale. The corresponding value projected in the source plane is $\eta_0=\zeta_0 D_\mathrm{s}/D_\mathrm{d}$ and the source position is $\vec{y}=\vec{\eta}/\eta_0$.

The dimensionless surface mass density $\kappa(x)$, also called *convergence*, is

$$\kappa(x) = \frac{\Sigma(x)}{\Sigma_\mathrm{cr}} \quad \text{with} \quad \Sigma_\mathrm{cr} = \frac{c^2}{4\pi G}\,\frac{D_\mathrm{s}}{D_\mathrm{d}D_\mathrm{ds}}\,. \quad (11)$$

The dimensionless ray-tracing equation is then,

$$\vec{y} = \vec{x} - \vec{\alpha}(\vec{x}) \,, \tag{12}$$

with the scaled deflection angle

$$\vec{\alpha}(\vec{x}) = \frac{D_{\rm d} D_{\rm ds}}{\zeta_0 D_{\rm s}} \vec{\delta}(\zeta_0 \vec{x}) = \frac{2}{x} \int {\rm d}x' \, x' \, \kappa(x') \,. \tag{13}$$

The axial symmetry of the lenses considered here allows us to rewrite the lens equation in terms of the dimensionless "mass" $m(x)$ enclosed within the radius x,

$$\vec{y} = \vec{x} - \frac{m(x)}{x} \,, \tag{14}$$

with

$$m(x) = 2 \int_0^x {\rm d}x' \, x' \, \kappa(x') \,. \tag{15}$$

The Jacobian matrix $A(\vec{x}) = \partial\vec{y}/\partial\vec{x}$ for the lens mapping [Eq. (14)] determines the magnification factor for each image i,

$$\mu_i = \frac{1}{\det A(\vec{x}_i)} \,. \tag{16}$$

The sign of μ_i reflects the parity of the image with respect to the source. The total source magnification is the sum of the absolute values of the magnification factors of all images,

$$\mu = \sum_i |\mu_i| \,. \tag{17}$$

For axially symmetric lenses, the Jacobian determinant of the lens mapping can also be written

$$\begin{aligned} \det A &= \left(1 - \frac{\alpha(x)}{x}\right) \left(1 - \frac{\rm d}{{\rm d}x}\alpha(x)\right) \\ &= \left(1 - \frac{m}{x^2}\right) \left[1 - \frac{\rm d}{{\rm d}x}\left(\frac{m}{x}\right)\right] = (1-\kappa)^2 - \gamma^2 \,, \end{aligned} \tag{18}$$

where γ is the shear (cf. Schneider, Ehlers & Falco 1992). Critical curves are located at the zeros of $\det A$; their images in the source plane under the mapping described by Eq. (12) are the caustics.

A simple model for the mass profile of a lens (cluster or galaxy) is the singular isothermal sphere (SIS; e.g. Binney & Tremaine 1987):

$$\rho(r) = \frac{\sigma_v^2}{2\pi G r^2} \,, \tag{19}$$

where σ_v is the line-of-sight velocity dispersion. In this case, the deflection angle is independent of the impact parameter (cf. Schneider et al. 1992; Narayan & Bartelmann 1997). One of the two critical curves degenerates to a point. Any given source has either one or two images. Two images appear only if the source lies inside the Einstein ring. The Einstein angle corresponding to a SIS is

$$\theta_{\rm E} = \hat{\alpha} \frac{D_{\rm ds}}{D_{\rm s}} \tag{20}$$

with

$$\hat{\alpha} = 4\pi \frac{\sigma_v^2}{c^2} = 1.4'' \left(\frac{\sigma_v}{220\,{\rm km\,s^{-1}}}\right)^2 \,. \tag{21}$$

In order to evaluate the mass of a halo with velocity dispersion σ_v from Eq. (19), we truncate the sphere at an effective radius computed following Lahav et al. (1991).

If every halo virializes to form a singular isothermal sphere, mass conservation implies that the velocity dispersion is related to the mass and to the virialization redshift by (see, e.g. Porciani & Madau 2000; Kaiser 1986):

$$\sigma_v = \frac{1}{2} H_0 \, r_0 \, \Omega_{\rm 0m}^{1/3} \Delta^{1/6} \left[\frac{\Omega_{\rm 0m}}{\Omega_{\rm m}}\right]^{1/6} (1+z)^{1/2} \tag{22}$$

where $\Omega_{\rm m}$ is defined in the previous section, $r_0 = (3M/4\pi\rho_0)^{1/3}$, and $\Delta(z)$ is the mean density of the virialized halo in units of the critical density at that redshift. A useful expression for the dependence of σ_v on redshift is given in Bryan & Norman (1998),

$$\sigma_v = M^{1/3} \left[H^2(z) \Delta(z) G^2/16\right]^{1/6} \,. \tag{23}$$

Bryan & Norman (1998) also give a fitting formula for $\Delta(z)$ for a flat universe with a cosmological constant and for a universe with $\Omega_{0R} \neq 0$ and $\Omega_\Lambda = 0$. For a flat universe, ($\Omega_{0R} = 0$) their hydrodynamical simulations yield:

$$\Delta(z) = 18\pi^2 + 82x - 39x^2 \,, \tag{24}$$

where $x = \Omega_{\rm m} - 1$.

The SIS model is useful because it allows to work out analytically the basic lensing properties. On the other hand, high-resolution N-body simulations (Navarro, Frenk & White 1997) showed that in hierarchically clustering universes, virialized dark matter halos have a universal density profile (referred to as NFW), which is shallower than isothermal near the center and steeper in the outer regions:

$$\rho(x) = \frac{\rho_{\rm crit} \delta_{\rm NFW}}{x\,(1+x)^2} \,, \tag{25}$$

where $x = r/r_{\rm s}$, $r_{\rm s}$ being a scale radius, $\delta_{\rm NFW}$ is the characteristic density contrast of the halo, and $\rho_{\rm crit}$ is the critical density at the epoch of the halo virialization. This formula was found to accurately describe the equilibrium density profiles of dark matter halos over a broad range of masses ($3 \times 10^{11} \leq M_{200}/M_\odot \leq 3 \times 10^{15}$), irrespective of the cosmological parameters and the initial density fluctuation spectrum.

Still higher resolution N-body simulations indicate a steeper central cusp than that of the NFW profile: $\rho(x) \propto \left[x^{1.5}(1+x)^{1.5}\right]^{-1}$ (Moore et al. 1999; Ghigna et al. 2000). Since the slope of the central density profile in this case [$\rho(r) \propto r^{-1.5}$] is intermediate between those of the NFW [$\rho(r) \propto r^{-1}$] and of the SIS [$\rho(r) \propto r^{-2}$], the two cases considered here (NFW and SIS) will bracket it.

We parameterize halos by their mass M_{200} (defined as the mass within the virial radius r_{200}, the radius of a sphere of mean interior density $200\rho_{\rm crit}$; see Navarro et al. 1997), since this is the mass whose distribution is given by Eq. (1). Unless otherwise specified, we abbreviate M_{200} by M. The halo concentration is $c = r_{200}/r_{\rm s}$. It is related to the density parameter $\delta_{\rm NFW}$ by

$$\delta_{\rm NFW} = \frac{200}{3} \frac{c^3}{[\ln(1+c) - c/(1+c)]} \,. \tag{26}$$

The virial radius of a halo at redshift z depends on the halo mass as

$$r_{200} = \frac{1.63 \times 10^{-2}}{(1+z)} \left(\frac{M}{h^{-1} M_\odot}\right)^{1/3} \left[\frac{\Omega_{\rm 0m}}{\Omega_{\rm m}(z)}\right]^{-1/3} h^{-1}\,{\rm kpc} \,. \tag{27}$$

Alternatively, the halo can be characterized by its circular velocity,

$$\begin{aligned} V_{200} &= \left(\frac{GM_{200}}{r_{200}}\right)^{1/2} \\ &= \left(\frac{r_{200}}{h^{-1}\,{\rm kpc}}\right) \left[\frac{\Omega_{\rm 0m}}{\Omega_{\rm m}(z)}\right]^{1/2} (1+z)^{3/2}\,{\rm km\,s^{-1}} \,. \end{aligned} \tag{28}$$

The scale radius $r_{\rm s}$ depends on the halo mass. The halo concentration increases with decreasing halo mass (e.g. Fig. 6 of Navarro et al. 1997). Less massive halos are therefore more concentrated.

For a given halo mass, Eqs. (27) and (26) completely specify the density profile [Eq. (25)].

The lens equations for the NFW profile are given by Bartelmann (1996) and Maoz et al. (1997). The surface mass-density is

$$\Sigma(x) = \frac{2\rho_{\rm crit}\delta_{\rm NFW}\, r_{\rm s}}{x^2-1}\, f(x)\ , \tag{29}$$

with

$$f(x) = \begin{cases} 1 - \frac{2}{\sqrt{x^2-1}} \arctan\sqrt{\frac{(x-1)}{(x+1)}} & (x>1) \\ 1 - \frac{2}{\sqrt{1-x^2}} \mathrm{arctanh}\sqrt{\frac{(1-x)}{(x+1)}} & (x<1) \\ 0 & (\mathrm{x}{=}1) \end{cases} . \tag{30}$$

The dimensionless lens mass is

$$m(x) = \frac{4\rho_{\rm crit}\delta_{\rm NFW}\, r_{\rm s}}{\Sigma_{\rm cr}}\, g(x)\ , \tag{31}$$

with

$$g(x) = \ln\frac{x}{2} + 1 - f(x)\ . \tag{32}$$

While the NFW profile [Eq. (25)] has two critical curves (Bartelmann 1996), the SIS profile has only one. A SIS lens has either one or two images, an NFW lens either one or three.

4 THE MAGNIFICATION BIAS

In this section, we follow the approach by Schneider et al. (1992) and Schneider (1987a,b). We call μ the magnification of fluxes in an inhomogeneous universe, and relate it to the magnification A in a homogeneous universe.

The effect of lensing on flux-limited source counts is quantified by the magnification bias (Turner et al. 1984). If the surface density of galaxies with flux greater than $S_{\rm v}$ is $N(S_{\rm v})$, flux magnification alters the counts to $N'(S_{\rm v}) = \mu^{-1} N(S_{\rm v}\mu^{-1})$, and the magnification bias is given by (Narayan 1989):

$$q(\mu, S_{\rm v}) = \frac{N'}{N} = \frac{N(S_{\rm v}\mu^{-1})}{\mu\, N(S_{\rm v})}\ . \tag{33}$$

The factor μ^{-1} arises because solid angles are magnified, hence source counts are diluted. Eq. (33) implies that for power-law counts ($N \propto S_{\rm v}^{-\alpha}$), $q(\mu, S_{\rm v}) = \mu^{\alpha-1}$, so that the magnification bias increases as the counts steepen.

Since the reference to "unlensed" counts has given rise to confusion in the literature, it is important to specify our model for light propagation in the universe when talking about the number of sources seen "in absence of lensing".

In Eq. (33), N is defined as the number count of sources that do not appear behind lenses. Because of energy conservation, the flux of these objects must be reduced compared to a homogeneous universe with the same average density. In other words, since lensing is caused by inhomogeneities, we have to deal with an inhomogeneous universe. While sources observed through lenses are magnified by a factor $\mu^+ > 1$ compared to a homogeneous universe, unlensed sources must be demagnified by $\mu^- < 1$. When comparing lensed to unlensed sources, the effective magnification is

$$\mu = \frac{\mu^+}{\mu^-} > 1 \tag{34}$$

(e.g. Schneider 1984, 1987a,b). This is the "empty beam approach" to light propagation (Dyer & Roeder 1973; Ehlers & Schneider 1986), in which light cones are devoid of clumped matter. The fraction of uniformly distributed matter is denoted by $\alpha_{\rm s}$, the smoothness parameter.

In this *on-average* homogeneous and isotropic universe, the average flux $\langle S\rangle$ from a source population at redshift z with luminosity L, must be equal to the corresponding flux $S_{\rm FL}$ that would be observed in a strictly uniform Friedman-Lemaître universe,

$$\langle S\rangle = S_{\rm FL} = \frac{L\,K(L,z)}{4\pi \bar{D}_{\rm L}^2(z)}\ , \tag{35}$$

where $\bar{D}_{\rm L}(z)$ is the luminosity distance in the uniform universe, and $K(L,z)$ is the K-correction. In general, it is not possible to compare mean fluxes of sources in these two different spacetimes. In particular, the notion of distance has no unique meaning in a clumpy universe, as it depends on both redshift and direction. Due to the corrugated structure of the gravitational field, the propagation of light in the inhomogeneous universe is a statistical problem. We can compare fluxes as in Eq. (35) only because we *assume* that the global geometry of the clumpy universe equals that of the homogeneous universe. Equation (35) implies that the area of a surface of constant redshift on the future light cone of a source is equal to that of the corresponding wavefront in the Friedman-Lemaître model. In order to use redshift-distance relations in an inhomogeneous, partly clumpy universe, which is uniform on average, it is then necessary to introduce a meaningful operational definition of distance. Since light propagation in a clumpy universe depends on the clumps in and near the light beam, Dyer & Roeder (1973) considered the limiting case of a light bundle that propagates far away from all clumps and is thus unaffected by gravitational shear. This is the "empty cone" limit.

The angular-diameter distance is then computed by replacing the density parameter $\Omega_{\rm m}$ with the "homogeneous" fraction $\alpha_{\rm s}\Omega_{\rm m}$. The resulting "Dyer-Roeder" distance is larger than the angular-diameter distance in a homogeneous universe. For a spatially-flat universe with deceleration parameter $q_0 = 0.5$, the Dyer-Roeder distance between redshifts z_1 and $z_2 > z_1$ is

$$r(z_1, z_2, \beta) = \frac{2}{\beta}\left[\frac{(1+z_2)^{(\beta-5)/4}}{(1+z_1)^{(\beta+5)/4}} - \frac{(1+z_1)^{(\beta-5)/4}}{(1+z_2)^{(\beta+5)/4}}\right]\ , \tag{36}$$

where $\beta = (1+24\Omega_{\rm G})^{1/2}$ and $\Omega_{\rm G} = (1-\alpha_{\rm s})\Omega_{\rm m}$ is the density parameter in compact objects ($\beta = \alpha_{\rm s} = 1$ for the homogeneous universe). Hereafter, we abbreviate $r(0,z,\beta) \equiv r(z,\beta)$ and $r(z,1) \equiv r_1(z)$. The dimensional angular diameter distance in a homogeneous universe is

$$D_1(z) = \frac{c}{H_0}\, r_1(z)\ . \tag{37}$$

The problem is more complicated when the cosmological constant is positive. The Dyer-Roeder equation in a FRW universe with non-zero cosmological constant has been solved exactly by Kantowski (1998), Kantowski & Kao (2000) and, following a different approach, by Demianski et al. (2000). The general solution can be expressed in terms of the hypergeometric functions $f_{s\pm}$ introduced by Demianski et al. (2000):

$$r(z,\beta) = A_1\,\frac{(1+z)^{-\beta/4}}{(1+z)^{5/4}}\,\frac{f_{s+}}{(1+z)^3} + A_2\,\frac{(1+z)^{\beta/4}}{(1+z)^{5/4}}\,\frac{f_{s-}}{(1+z)^3}\ , \tag{38}$$

where the constants $A_{1,2}$ are determined by the boundary conditions

$$r(z,\beta)|_{z=0} = 0 \quad \text{and} \quad \left.\frac{{\rm d}r}{{\rm d}z}\right|_{z=0} = 1\ . \tag{39}$$

This can be used to generalize the two-point distance of Eq. (36), which, for a non-zero cosmological constant, reads:

$$r(z_1,z_2,\beta) = r(z_1,\beta)(1+z_1)r(z_2,\beta) \times \int_{z_1}^{z_2} \mathrm{d}z' \, \frac{[(1+z')^3\Omega_{0\mathrm{m}}+\Omega_{0\Lambda}]^{1/2}}{r^2(z',\beta)(1+z')^2} \, , \quad (40)$$

with $r(z,\beta)$ given by Eq. (38).

For practical applications, these exact solutions are rather cumbersome to use. Demianski et al. (2000) give approximate solutions for $r(z,\beta)$ and $r(z_1,z_2,\beta)$, which we use in this paper in the form kindly provided by R. de Ritis (private communication) for $\Omega_{0\Lambda}=0.7$ and $\alpha_s=0.9$, implying $\beta=1.84$, and $\Omega_G=0.1$. We ignore a possible time-dependence of the smoothness parameter. The effect of different choices of α_s on the Dyer-Roeder distance with positive cosmological constant is shown in Demianski et al. (2000).

Having introduced the Dyer-Roeder distance, we can interpret the magnification in Eq. (34) as the ratio between the flux S actually received from a source at redshift z, and the flux S_{empty} that would be received if the same source was observed through an empty cone:

$$\mu = \frac{S}{S_{\mathrm{empty}}} = S\frac{4\pi D_{\mathrm{L}}^2(z,\beta)}{LK(L,z)} > 1 \, , \quad (41)$$

where

$$D_{\mathrm{L}}(z,\beta) = \frac{c}{H_0}(1+z)^2 \, r(z,\beta) \quad (42)$$

is the luminosity distance in an empty cone.

Since the clumpy universe is homogeneous on-average, $\bar{D}_{\mathrm{L}}(z,\beta) = D_{\mathrm{L}}(z,1)$. Using Eq. (41), Eq. (35) reads

$$\langle\mu\rangle = \left(\frac{r(z,\beta)}{r_1(z)}\right)^2 > 1 \, . \quad (43)$$

$\langle\mu\rangle$ can be interpreted as the magnification of an average light beam in a smooth universe relative to that for an empty cone in a clumpy universe: $\langle\mu\rangle = S_{\mathrm{FL}}/S_{\mathrm{empty}}$.

For $q_0 = 1/2$, $\langle\mu\rangle$ becomes

$$\langle\mu\rangle = \beta^{-2}\frac{\sinh^2[0.25\beta\ln(1+z)]}{\sinh^2[0.25\ln(1+z)]} \, , \quad (44)$$

(Pei 1993b), while for the more general case including the cosmological constant, $\langle\mu\rangle$ has to be derived from Eq. (43).

Let $p(\mu,z)\mathrm{d}\mu$ denote the probability for a source at redshift z to be magnified by a factor of μ within $\mathrm{d}\mu$. The normalization and flux conservation conditions require:

$$\int_1^\infty \mathrm{d}\mu \, p(\mu,z) = 1 \, , \quad \int_1^\infty \mathrm{d}\mu \, p(\mu,z)\mu = \langle\mu\rangle \, . \quad (45)$$

When dealing with source counts on cosmological scales, however, it is often convenient to refer magnifications to the homogeneous universe rather than to the "demagnified" background. We call A the magnification relative to the homogeneous universe:

$$A = \frac{S}{S_{\mathrm{FL}}} = \frac{S_{\mathrm{empty}}}{S_{\mathrm{FL}}}\mu \, , \quad (46)$$

where $\mu = S/S_{\mathrm{empty}}$ is the magnification of a source seen through an empty beam, as in Eq. (41). Eqs. (35) and (43) imply:

$$A = \frac{\mu}{\langle\mu\rangle} \, . \quad (47)$$

This is the definition of magnification used, for example, by Blain (1996) and Peacock (1982). It is trivial to show that for a given source redshift z, $p(\mu,z)\mathrm{d}\mu = p(A,z)\mathrm{d}A$, and the normalization and flux conservation conditions become

$$\int_{A_{\mathrm{min}}}^\infty \mathrm{d}A \, p(A,z) = 1 \, , \quad \int_{A_{\mathrm{min}}}^\infty \mathrm{d}A \, p(A,z)A = 1 \, . \quad (48)$$

Here, A_{min} is the minimum magnification relative to the FRW universe, that can be produced by compact lenses, i.e. $A_{\mathrm{min}} = \langle\mu\rangle^{-1}$. Since $\langle A\rangle = 1$, the sources which are demagnified with respect to the homogeneous universe have $A < 1$.

5 THE MAGNIFICATION DISTRIBUTION

The number of images produced by a lens, their angular separation and their magnification depend on their relative alignment as seen by the observer. For a fixed geometry of the lens system, one can ask where the source must lie for its images to have a total magnification larger than a given value μ. The area of the resulting region in the source plane is the cross section $\sigma(\mu,z_{\mathrm{d}},z_{\mathrm{s}},\chi)$, which obviously depends on lens and source redshifts, z_{d} and z_{s}, on a set of parameters χ describing the lens model, and on the magnification itself. As both SIS and NFW halos are completely characterized by their mass, $\chi = M$ here. The cross section quantifies the efficiency of the individual lens on a source. It is generally found numerically, by solving the lens equation and finding the area in the source plane where a source must lie in order to produce images with a total magnification larger than μ_{tot}. The cross section of a singular isothermal sphere for a total magnification $\mu_{\mathrm{tot}} > \mu$ is

$$\sigma(\mu_{\mathrm{tot}} > \mu) = \frac{4\pi\hat{\alpha}^2 D_{\mathrm{ds}}^2}{\mu^2} \quad \text{for} \quad \mu \geq 2 \, . \quad (49)$$

We need to compute the total magnification cross section of an ensemble of lenses distributed according to the mass function of Eq. (1). We denote by $n_{\mathrm{c}}(z,M)$ the comoving lens number density, and $n(z,M) \equiv (1+z)^3 n_{\mathrm{c}}(z,M)$. As long as the cross sections of individual lenses do not overlap, each light bundle from a source encounters only one lens, and the total cross section is the integral of the individual cross sections over the redshift and mass distributions of lenses:

$$\sigma_{\mathrm{tot}}(\mu,z_{\mathrm{s}}) = 4\pi\left(\frac{c}{H_0}\right)^3 \times \int_0^{z_{\mathrm{s}}} \mathrm{d}z \int \mathrm{d}M \, \frac{\sigma(\mu,z,z_{\mathrm{s}},M)\, n_{\mathrm{c}}(z,M)\,(1+z)^2\, r_1^2(z)}{\sqrt{\Omega_{0\mathrm{m}}(1+z)^3+\Omega_{0\Lambda}}} \, , \quad (50)$$

where the proper volume of a spherical shell of width $\mathrm{d}z$ at redshift z is

$$\mathrm{d}V = 4\pi\left(\frac{c\,r_1(z)}{H_0}\right)^2 \times \frac{\mathrm{d}r_{\mathrm{prop}}}{\mathrm{d}z}\,\mathrm{d}z \, . \quad (51)$$

For a spatially-flat universe

$$\frac{\mathrm{d}r_{\mathrm{prop}}}{\mathrm{d}z} = \frac{c}{H_0\,(1+z)\,\sqrt{\Omega_{0\mathrm{m}}(1+z)^3+\Omega_{0\Lambda}}} \, . \quad (52)$$

The probability for a source at redshift z_{s} to be lensed with magnification $> \mu$ is obtained by dividing σ_{tot} by the area of the source sphere

$$P(\mu,z_{\mathrm{s}}) = \frac{c}{H_0}\,\frac{1}{r_1^2(z_{\mathrm{s}})}\int_0^{z_{\mathrm{s}}} \mathrm{d}z \, \frac{r_1^2(z)\,(1+z)^2}{\sqrt{\Omega_{0\mathrm{m}}(1+z)^3+\Omega_{0\Lambda}}} \cdot \int \mathrm{d}M\,\sigma(\mu,z,z_{\mathrm{s}},M) n_{\mathrm{c}}(z,M) \, . \quad (53)$$

The requirement of non-overlapping cross sections restricts the validity of Eq. (53) to $P \ll 1$, i.e. the total cross section must be much smaller than the area of the source sphere. The net effect of gravitational lensing on the distribution of flux densities expected from a population of distant sources can be described by the probability distribution of magnifications, $p(\mu,z)$ introduced in Sect. 4. While $P \ll 1$, the differential probability is $p(\mu,z) = -\mathrm{d}P(\mu,z)/\mathrm{d}\mu$; in particular, $p(A,z) = p(\mu,z)\langle\mu\rangle$.

The differential probability decreases as μ^{-3} for $\mu \gg 1$, hence the high magnification tail in terms of A can be written as $p(A,z) \propto a(z)A^{-3}$. On the other hand, Eq. (53) breaks down for small magnifications, where multiple lensing events become important and cross sections overlap (in fact, the probability for many low-magnification lensing events along the line of sight to a source is rather large, while a single interaction producing high magnifications is a relatively rare event). In particular, this implies that there is a critical magnification $A_{\rm cut}$ below which multiple lensing becomes important, resulting in low-magnification events (weak lensing regime). Vietri & Ostriker (1983) analytically described multiple lensing for the SIS model.

Based on general considerations (see Bartelmann & Schneider 2001 for a review), one expects a skewed magnification distribution with a weak lensing peak near $A = 1$, turning into the high-magnification tail $\propto A^{-3}$ at $A = A_{\rm cut}$.

For a Gaussian density fluctuation field δ, weak lensing by large scale structure (e.g. Bartelmann & Schneider 2001; Miralda-Escudé 1991; Blandford et al. 1991; Kaiser 1992; Jain & Seljak 1992) produces a Gaussian magnification distribution. In fact, as long as $\delta A \equiv A - 1 \ll 1$, the magnification of a source at redshift z can be approximated as

$$A(z) = 1 + \delta A(z) \approx 1 + 2\kappa(z) \; , \tag{54}$$

i.e. to first order the magnification fluctuation is just twice the convergence κ, which itself is a projection of the density contrast δ. The distribution of the magnification fluctuations δA will then be Gaussian, with mean zero and a dispersion $\sigma_{\rm A}(z)$ which depends on the source redshift and, albeit weakly, on cosmology. Typical values for $\sigma_{\rm A}$ run from $\sim 2\times10^{-3}$ for $z = 0.05$ to ~ 0.44 at $z = 7.5$ (cf. Bartelmann & Schneider 2001).

A convenient choice for $A_{\rm cut}$ is $A_{\rm cut} = 1 + 1.5\sigma_{\rm A}(z)$, yielding $A_{\rm cut} \approx 1.5 - 2$ for the redshift range of interest in this paper. We model the probability distribution for $A < A_{\rm cut}$ as

$$p(A,z) = H(z)\,\exp[-(A-\bar{A})^2/2\sigma_{\rm A}^2(z)] \; , \tag{55}$$

where the precise location of the peak $\bar{A}$ and the amplitude $H(z)$ are determined by the normalization and flux conservation conditions [Eq. (48)] on the *combined* (weak plus strong lensing) probability distribution.

The magnification probability for isothermal galaxy models has been derived by Peacock (1982) and Vietri & Ostriker (1983), and, for more complicated galaxy models, by Blandford & Kochanek (1987) and Wallington & Narayan (1993). In this paper, we integrate Eq. (53) also for lenses with NFW density profile (see Sect. 3), and we describe the low-magnification distribution according to Eq. (55). Numerical results are presented in Section 8.

Let us now turn to the magnification bias on a flux-limited source sample. The integrated counts above a flux density threshold S_ν of sources with a comoving luminosity function $\Phi(L,z)$ can be written as (see e.g. De Zotti et al. 1996):

$$N(S_\nu) = \int_0^{z_0} \mathrm{d}z \int_{L_{\rm min}}^{\infty} \mathrm{d}L\,\Phi(L,z)\,\frac{D_{\rm L}^2(z,1)}{(1+z)^2}\,\frac{\mathrm{d}r}{\mathrm{d}z} \qquad \mathrm{sr}^{-1}, \tag{56}$$

where the luminosity distance $D_{\rm L}^2(z,1)$ is computed from Eq. (42) with $\beta = 1$ and

$$L_{\rm min}(\nu) = 4\pi(1+z)\,r^2(z)\,S_\nu\,\frac{L(\nu)}{L[(1+z)\nu]} \; . \tag{57}$$

Note that the comoving radial coordinate r [and its element dr in Eq. (56)] must not be confused with the dimensionless angular diameter distance $r_1(z)$ [Eq. (37))].

The luminosity function modified by the magnification bias reads (e.g. Pei 1995):

$$\Phi'(L,z) = \int_{A_{\rm min}}^{\infty} \mathrm{d}A\,\frac{p(A,z)}{A}\,\Phi\left(\frac{L}{A},z\right) \; . \tag{58}$$

Allowance for the effect of lensing on counts is made by replacing $\Phi'(L,z)$ to $\Phi(L,z)$ in Eq. (56).

6 SOURCE COUNTS IN THE SUBMILLIMETRE WAVEBAND

In this paper, the "unlensed" galaxy counts in the submillimetre waveband are taken from the model presented by Granato et al. (2000), which is in good agreement with the available SCUBA data at 850 μm (Blain et al. 1999; Smail et al. 1999).

In this model the rate of formation of spheroids at high redshift is estimated exploiting the (i) QSO Luminosity Function and (ii) observational evidence leading to the conclusion that high redshift QSOs did shine in the core of early type proto–galaxies during their main episode of star formation. In their scenario the star formation is more rapid in more massive objects, ranging from ~ 0.5 to ~ 2 Gyr when going from more massive to less massive objects. This *Anti-hierarchical Baryonic Collapse* is expected to occur in Dark Matter halos, when the processes of cooling and heating is considered. The larger the dark halo and the enclosed spheroid mass are, the shorter will the gas infall and cooling times be, resulting in a faster formation of the stars and of the central black hole. The star-formation process and the quasar shining phase proceed until powerful galactic winds are caused by the quasar itself, which occurs at a characteristic time when its luminosity becomes high enough. Also Monaco et al (2000), in order to account for the observed statistics of QSOs and elliptical galaxies in the framework of hierarchical structure formation, introduced a a time delay decreasing with mass between the beginning of the star formation and the QSO bright phase.

The spectroscopic evolution of galaxies adopted here is based on the model GRASIL (Silva et al. 1998). GRASIL includes: (*i*) chemical evolution; (*ii*) dust formation, assumed to follow the chemistry of the gas; (*iii*) integrated spectra of simple stellar populations (SSP) with the appropriate chemical composition; (*iv*) realistic 3D distribution of stars, molecular clouds (in which stars form and subsequently escape) and diffuse dust; (*v*) radiative transfer computation in this clumpy ISM and dust temperature distribution determined by the local radiation field.

With these ingredients, the evolving luminosity functions (LF) at various wavelengths in the millimeter and submillimetre wavebands are evaluated numerically, and they turn out to be significantly different from models of Pure Luminosity Evolution for the 60 μm LF of IRAS galaxies (Saunders et al. 1990), properly rescaled to the wavelengths of interest. The IRAS galaxy LF, which is based on an empirical model describing the evolution in a parametric way, was used by Blain (1996) to obtain galaxy counts in the submillimetre wavebands, which were then used for estimating the

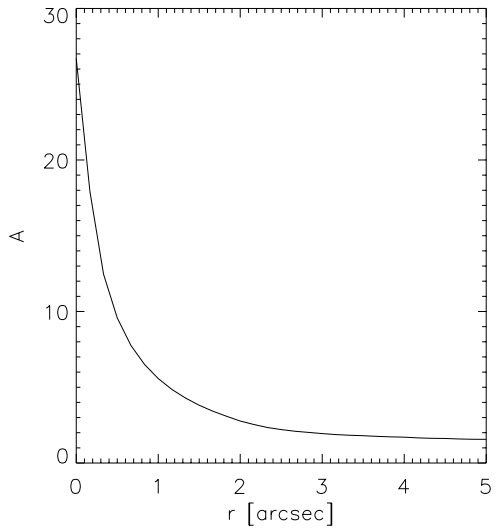

Figure 1. Magnification of an extended source as a function of the offset r between its center and the projection of the lens center in the source plane. Here the lens potential has no ellipticity. See text for details.

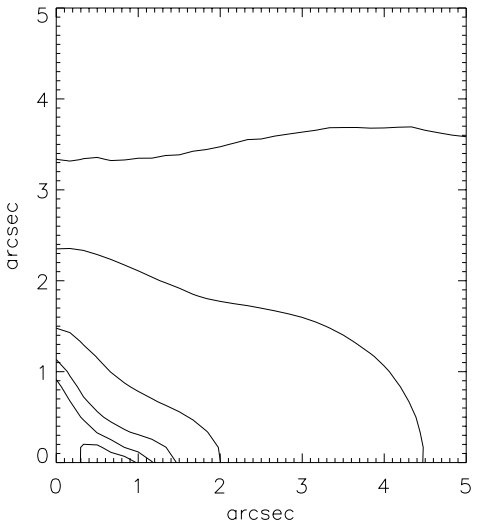

Figure 2. Contour plot of the magnification for an extended source when $g = 0.1$. The projection of the lens center in the source plane is at the origin of axes. The levels are at $A = 1.5, 2, 4, 6, 8, 10$ from outside in. See text for details.

incidence of gravitational lensing on source counts. However, the model by Granato et al. implies steeper source counts, nearly exponentially decreasing at bright fluxes, so that, as explained in section (4), the effect of gravitational lensing is expected to be more important.

All source counts obtained in this paper, with and without magnification bias, the spheroids include elliptical galaxies as well as bulges of Sa galaxies, and we followed the formalism of Granato et al. (2000) on the source properties.

7 MAXIMUM MAGNIFICATION FOR EXTENDED SOURCES

As discussed by Peacock (1982), in the case of extended sources the magnification cannot be arbitrarily large. Correspondingly the magnification distribution must be cut-off at large A as:

$$p(A) \propto \exp\left(-\frac{A}{A_{\max}}\right) , \tag{59}$$

where the cut-off magnification $A_{\max}$ depends on the physical size of the source.

Since, in some applications, e.g. for the estimate of the influence of lensing on counts of sub-millimeter sources (Blain 1996), the results are sensitive to the adopted value of $A_{\max}$, the approximated expression derived by Peacock (1982) [$A_{\max} = 70(DH_0/c)(d/\mathrm{kpc})^{-1}$, where d is the physical radius of the source, D is the angular diameter distance of the source and c/H_0 is the Hubble radius] may not be sufficient.

The morphology of strongly lensed sources indicates that most lenses are not circularly symmetric (e.g. Narayan & Bartelmann 1997 and references therein). Therefore, to estimate the maximum possible magnification for a source of physical radius r at redshift z_s, we considered in general an elliptical lensing potential due to a quasi isothermal sphere (Blandford & Kochanek 1987). Defining polar coordinates r and θ in the image plane, with origin at the center of mass, and measuring θ from the major axis of the ellipse, the deflection potential may be written as:

$$\Psi(r,\theta) = \theta_{\mathrm{E}}\sqrt{(s^2+r^2)}(1-g\cos 2\theta) . \tag{60}$$

Here g is the ellipticity parameter, s the core radius and θ_{E} is defined by Eq. (20). The results for an extended source are weakly dependent on s, within a relatively broad interval; therefore we simply set $s = 0$ in the following. With this potential we have computed the expected magnification of a pointlike source $A(\vec{y})$, as a function of its position $\vec{y}$ in the source plane. This has been done by means of the ray-shooting method (e.g. Schneider et al. 1992, pag. 304). Then the magnification of an extended source with brightness profile $I(\vec{y})$, as a function of the position $\vec{y}_E$ of its center, is given by

$$A_E(\vec{y}_E) = \frac{\int I(\vec{y})A(\vec{y})\,d^2y}{\int I(\vec{y})\,d^2y} . \tag{61}$$

For the brightness profile, we have used either a de Vaucouleurs law

$$\log I(R) = \log I_e - 3.33\left[(R/R_e)^{1/4} - 1\right] , \tag{62}$$

or the Hubble profile

$$I(R) = I_o/(1+R/R_o)^2 . \tag{63}$$

Observed profiles of spheroidal galaxies are well reproduced by both functional forms over a wide range of R, provided that $R_e \simeq 11\,R_o$ (Mihalas & Binney 1981).

We find that, adopting this relationship between the scale-lengths, the estimated A_E are very similar in both cases. Therefore in the following we present only results for Eq. (62). We assume in particular $R_e = 5$ kpc, typical for a bright elliptical galaxy (e.g. Kent 1985). For a SIS, the maximum possible magnification is achieved when the lens is local, i.e. when $D_{\mathrm{ds}} = D_{\mathrm{s}}$ in Eq. (20). We set $\sigma_v = 300$ km s^{-1}, which corresponds to a mass of 10^{12} M$_\odot$ within 25 kpc adopting the isothermal relationship $M(<R) = 2\sigma_v^2 R/G$. With our adopted cosmology, Eq. (20) yields $\theta_E = 2.6''$.

Figure 1 shows the corresponding magnification for an extended source as a function of the offset r between its center and

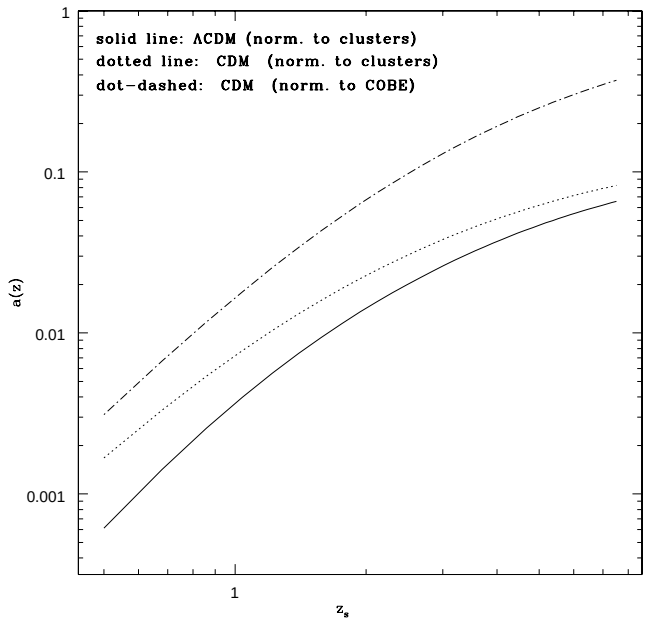

Figure 3. SIS model: comparison of the high-magnification tail amplitudes $a(z)$ for a flat ΛCDM model with $\Omega_\Lambda = 0.7$ (solid line), and a flat CDM model (dotted line), both normalized to the cluster abundance. The amplitude is plotted vs. source redshift. The dot-dashed line refers to a COBE-normalized flat CDM universe.

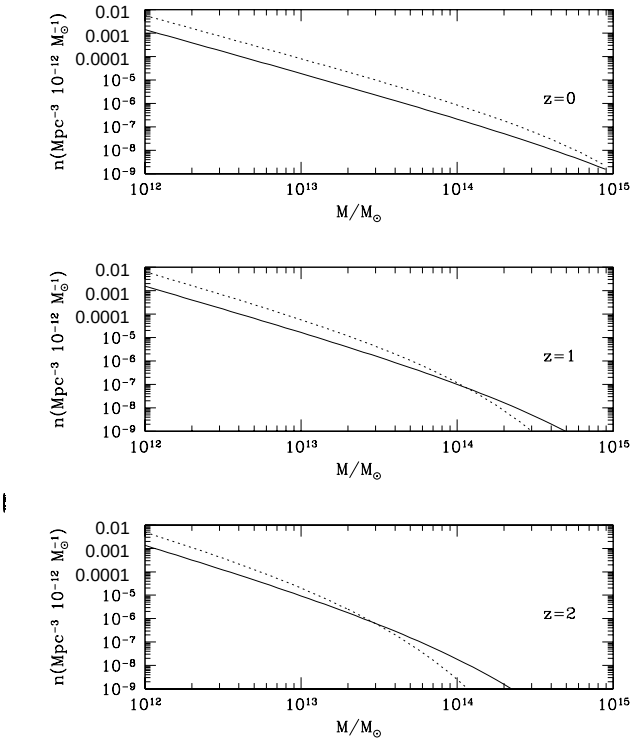

Figure 4. The Sheth & Tormen (1999) mass function for a flat CDM model (dotted line) and for a ΛCDM model (solid line), at redshifts $z = 0, 1, 2$, respectively, from top to bottom.

the projection of the lens center in the source plane. Here we have set $g = 0$ into Eq. (60), i.e. we adopt a spherical potential, and the source is at $z_s = 3$, but very similar plots are obtained for z_s in the range $1 \div 4$. As can be seen, the magnification is maximized when the source and the lens are aligned and $A_{\max} \simeq 26$. If the lens is placed instead at $z_l = 0.5$, then $b = 1.2$ arcsec and $A_{\max} \simeq 13$.

However, as already remarked, strongly lensed sources are usually explained in terms of potentials with non vanishing ellipticity. A typical value for g could be 0.1. In this case the symmetry of A_E around $r = 0$ is lost and the maximum magnification, $A_{\max} \simeq 12$, significantly lower than in the spherical case, occurs when the lens and the source are offset by $\sim 0.7''$ along the major axis of the ellipse. The results are detailed in Fig. 2.

We conclude that reasonable values of $A_{\max}$ for extended sources are in the range 10–30. The lower value is a relatively conservative lower limit, easily exceeded for a wide range of values for the relevant quantities, while the latter is obtained only under rather special conditions.

8 NUMERICAL RESULTS AND DISCUSSION

8.1 Effects from cosmology

To illustrate the effect of the cosmological model on the magnification probability distribution $p(A,z)$, we plot in Fig. 3 the amplitude $a(z)$ of the high-magnification tail for two different cosmologies, viz. a flat CDM and a ΛCDM model with $\Omega_{0\Lambda} = 0.7$ and $\Omega_{0m} = 0.3$. We have adopted SIS profiles for lenses and a smoothness parameter $\alpha_s = 0.9$. The two models are normalized to reproduce the local abundance of rich clusters: $\sigma_8 = 0.56\Omega_{0m}^{-0.47}$ (Viana & Liddle 1999).

The optical depth for a beam of light from a source due to lensing is proportional to the number density of deflectors multiplied by the cross section for a given magnification, integrated along the line of sight. Two competing effects are therefore relevant. On one hand, the path length to a source is larger for a ΛCDM model. On the other hand, the structure formation histories within the standard hierarchical clustering scenario are also different for the different cosmologies. If we normalize the models to reproduce the local cluster abundance, the density of lower mass objects is lower in the ΛCDM model, because the mass function is flatter (e.g. Eke et al. 1996). This is shown in the upper panel of Fig. 4, where the mass function [Eq. (1)] is plotted as a function of the halo mass at $z = 0$. The number of low-mass objects keeps increasing with redshift above the ΛCDM model, while the opposite is true for high masses.

The next question is then: which is the mass range contributing most to the optical depth? In Fig. 5 we show as a function of the lens mass, both the cross section for magnifications $A > 2$ and the lens mass function for given values of the source and lens redshifts. A SIS profile is adopted. It may be noted that the magnification cross section is similar for the two models (although slightly higher for the flat CDM model). The product of the two functions peaks at masses between 10^{11} and $10^{12}\,M_\odot$ for both a flat CDM and a ΛCDM model.

The effective mass of dark matter halos contributing most to strong lensing of a source located at z_s can be estimated as:

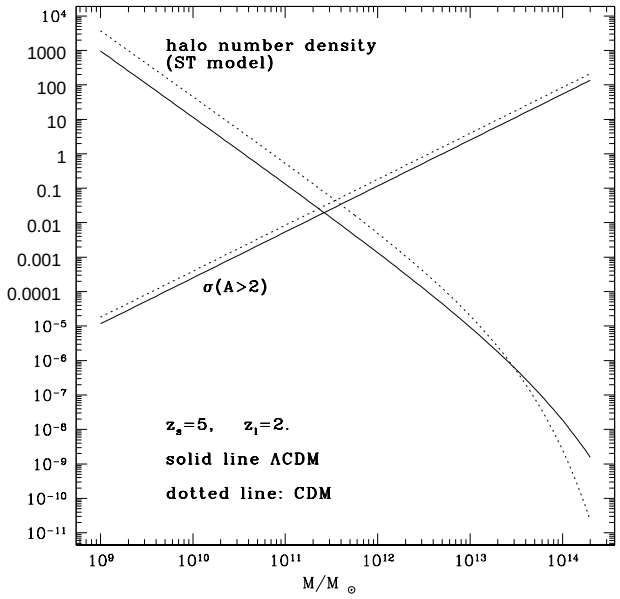

Figure 5. Number density of dark-matter halos (from the Sheth & Tormen mass function), and cross section for magnification $A > 2$ by a SIS lens, in arbitrary units, as a function of the lens mass in $M_\odot$. Dotted lines correspond to flat CDM, solid lines to ΛCDM, both normalized to the cluster abundance.

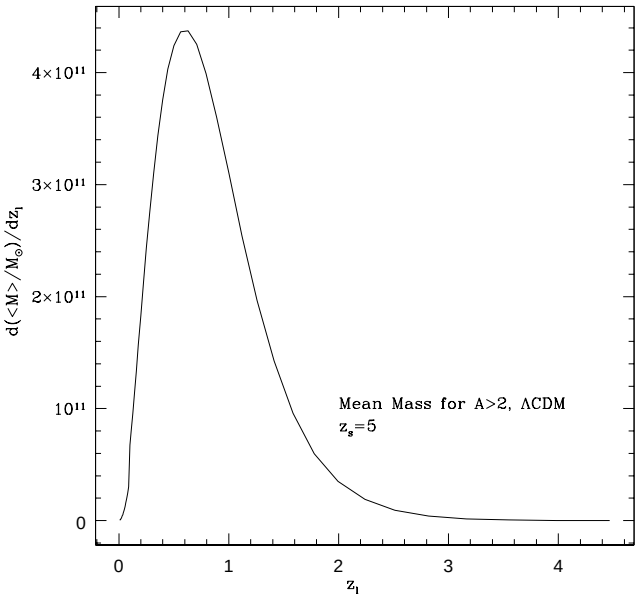

Figure 6. Contributions from different redshifts to the effective lens mass (see text) for a fixed configuration of the lens system, SIS lenses, and a ΛCDM model.

$$\langle M\rangle = \int \mathrm{d}z_\mathrm{l} \int \mathrm{d}M\, M\, \frac{\mathrm{d}P(A,z_s)}{\mathrm{d}z_\mathrm{l}\mathrm{d}M}\ , \tag{64}$$

where $P(A,z_s)$ is the probability to have magnification $> A$. The inner integral, $\mathrm{d}\langle M\rangle/\mathrm{d}z_\mathrm{l}$, is plotted as a function of z_l, for $z_s = 5$, a SIS lens profile and a ΛCDM model, in Fig. 6. As illustrated by this Figure, the maximum contribution to the magnification probability comes from the mass range (10^{11}–$10^{12}\,M_\odot$) for which space densities implied by a CDM model are appreciably higher than in the case of a ΛCDM model, in the relevant redshift interval, if the models have to be consistent with the observed cluster abundance. This over-compensates for the larger path length to a source in a ΛCDM model and explains why the probability distribution of strong magnifications has a *lower* amplitude for such model.

It may be noted (Fig. 3) that the difference between the two cases decreases with increasing source redshift, since also the ΛCDM model approaches an Einstein-de Sitter universe at high redshift.

Also shown in Fig. 3 is the amplitude $a(z)$ for a COBE-normalized standard-CDM model. The relatively large values for this quantity for any source redshift are unrealistic since they are due to a mass function of dark halos inconsistent with the cluster abundance.

8.2 SIS versus NFW profiles

Figure 7 compares the effect of SIS and NFW lens profiles on the magnification distributions for sources at $z_s = 4$ and $z_s = 7$, including the weak lensing effect for $A < A_\mathrm{cut}$. The magnification distributions are obtained by integrating over lens masses the cross sections in the source plane, weighted by the mass distribution [Eq. (1)]. The weak-lensing regime, responsible for magnifications below A_cut, gives rise to a Gaussian peak near $A = 1$ whose dispersion increases with increasing source redshift. In the strong-lensing regime, the probability distribution is obtained by solving Eq. (12) numerically and inserting the result in Eq. (53). The asymptotic behaviour $\propto A^{-3}$ is reached earlier by the most distant sources. The high-magnification tail of Fig. 7 is shown in closer detail in Fig. 8. Note that the plotted distribution of magnifications has a discontinuity in A_cut, i.e. at the transition between the weak and strong lensing regimes.

The two density profiles lead to slightly different magnification distributions. In particular, the NFW lens is more efficient than the SIS for moderate magnifications ($2 \lesssim A \lesssim 4$), and less efficient for high magnifications. In fact, NFW lenses have smaller high-magnification cross sections than SIS lenses of equal mass, even if the average magnification is higher. This can be read off Fig. 9, where we plot the cross section for magnifications $A > 2$ and $A > 10$ as a function of the halo mass for the two models, keeping fixed the configuration of the system. For virtually all halo masses, $\sigma(10)_\mathrm{NFW} < \sigma(10)_\mathrm{SIS}$, while $\sigma(2)_\mathrm{NFW} > \sigma(2)_\mathrm{SIS}$. Even though the latter relation fails for very small lens masses, it still holds when the cross sections are weighted with the appropriate mass function. As mentioned above, the bulk of the contribution to the magnification distribution comes from a limited mass range. The effective mass defined in Sect. 8.1 is nearly equal for SIS and NFW profiles, namely $\sim 10^{11-12} M_\odot$. Although $\langle M\rangle$ depends (albeit weakly) on

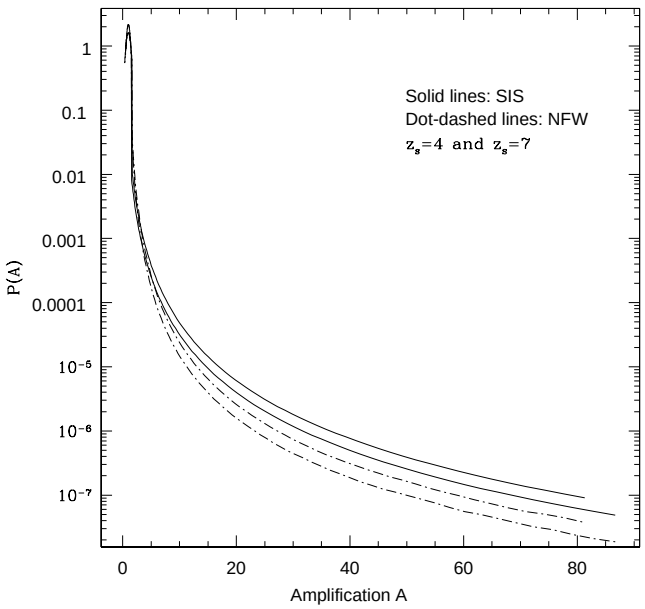

Figure 7. Magnification distribution from a population of SIS (solid lines) and NFW lenses (dot-dashed lines) for sources at redshifts $z_s = 4$ (lower curves) and $z_s = 7$ (upper curves).

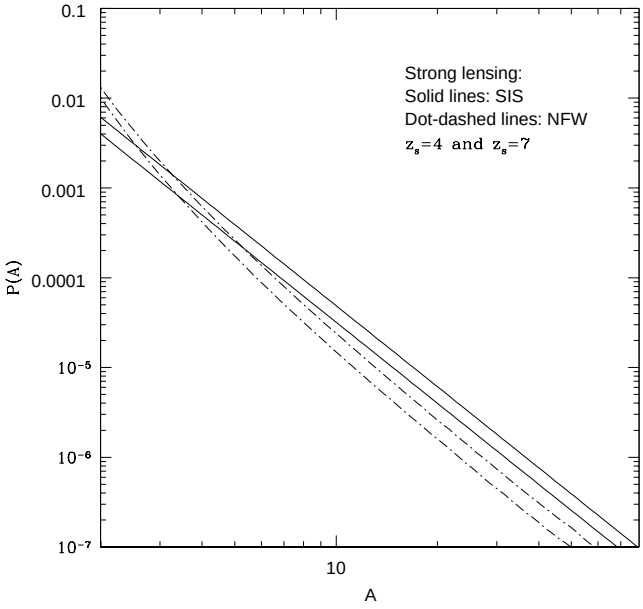

Figure 8. High-magnification tail of $P(A)$. Magnifications are plotted on a logarithmic scale. The plots refer to populations of SIS (solid lines) and NFW lenses (dot-dashed lines) for sources at redshifts $z_s = 4$ (lower curves) or at $z_s = 7$ (upper curves).

the lens redshift, massive clusters never contribute substantially to the integrand in Eq. (53) because they are extremely rare.

The SIS and NFW density profiles and the corresponding mass encompassed within the radius r for a $10^{12}\,M_\odot$ object are shown in Fig. 10. Virial radii are approximately equal in the two cases. For the NFW profile, the virial and scale radii are $r_{200} \simeq 140\,h^{-1}$ kpc and $r_s \simeq 15\,h^{-1}$ kpc, respectively, for $h = 0.65$; the concentration is $c \simeq 10$. The convergence κ for the two profiles is shown in the upper panel of Fig. 11 as a function of halocentric distance. Unlike the surface density, the convergence depends also on the geometry of the lens system. Here, the lens is at $z_l = 1$ and the source at $z_s = 5$. The two convergence profiles are quite similar, but the shear is also playing a fundamental role to determine the magnification distribution. In the lower panel of Fig. 11, we plot, for the two profiles, $\det^{-1} A$, i.e. the image magnification μ of an image with impact parameter r in the lens plane. Note that, even if some images are demagnified by lensing, the total magnification of the source is always > 1 (e.g. Schneider et al. 1992). The critical curves behave differently. Even though the NFW profile has a singular core, it has tangential and radial critical curves (Bartelmann 1996), while the SIS has only a tangential critical curve (whose caustic degenerates to a point for all axially symmetric lenses). Consequently, the maximum image number is two for SIS and three for NFW lenses.

Figure 11 shows that the tangential critical curve of a SIS occurs at a larger radius than both critical curves of an NFW halo with equal mass. This means that high magnifications are favored in the SIS model, because the corresponding cross sections in the source plane is larger. On the other hand, the SIS profile yields lower total magnifications when the source lies well outside the outer caustic in the source plane. The NFW cross sections for $\mu_{\rm tot} \sim 2$ generally overcome the SIS ones, due to the fact that the lensing potential is less curved for the NFW than for the SIS profile, hence this also occurs for more massive halos. In Fig. 12, we plot the equilibrium configurations for a $10^{14}\,M_\odot$ halo. The NFW profile has virial and scale radii of $r_{200} \simeq 690\,h^{-1}$ kpc and $r_s \simeq 100\,h^{-1}$ kpc, respectively, for $h = 0.65$ (the concentration is $c \simeq 6.5$).

In Fig. 13, we plot the convergence and the magnification for a single image as a function of its location. After adding all image magnifications, inverting to find the cross section $\sigma(\mu)$ vs. source position, and integrating over all lenses up to the source redshift, this explains the enhancement of the NFW probability for low magnifications with respect to the SIS model, shown in Fig. 7, and the opposite effect for large magnifications. However, we see that the probability distributions are quite similar and the effects of lensing on a source population turn out to be nearly identical for lenses with the two density profiles.

We finish with a cautionary note. The simulations resulting in the density profile of Eq. (25) did not have sufficient resolution for halo masses $\lesssim 10^{10}\,h^{-1}\,M_\odot$. We are therefore extrapolating the validity of this density profile as well as the relation between halo concentration and mass to a mass range where higher-resolution N-body simulations would be required. Furthermore, as Porciani & Madau (2000) pointed out, in order to obtain agreement with the data on image separations of QSOs one should consider baryonic cooling in dark matter halos, able to transform NFW halos into isothermal distributions for masses smaller than some threshold. In such a picture, DM halos are modeled as NFW halos only above a

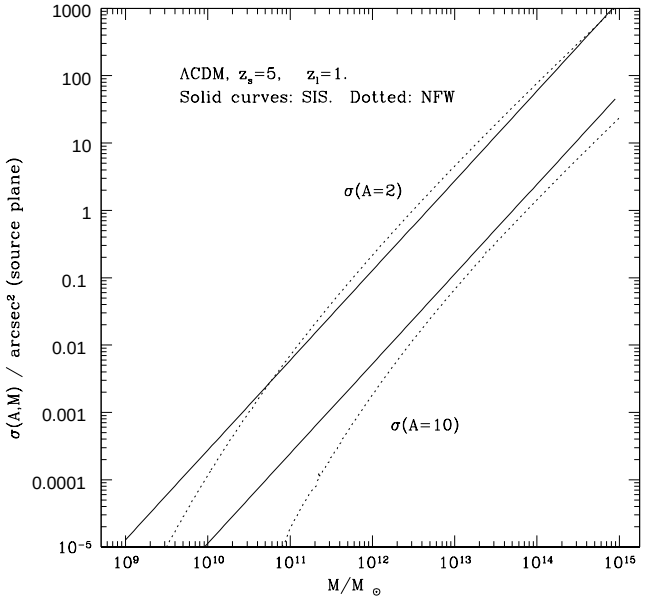

Figure 9. Magnification cross sections $\sigma(A)$ (in square arcsec) for $A > 2$ (upper curves) and $A > 10$, as a function of the halo mass. The sources are at $z_s = 5$ and the lenses at $z = 1$. The cross sections are plotted for SIS (solid lines) and NFW halos (dotted lines)

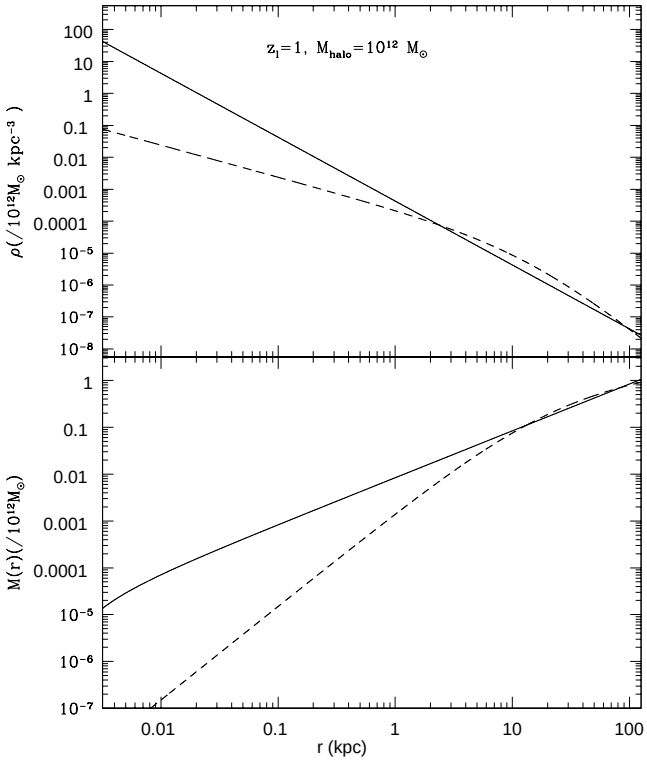

Figure 10. Upper panel: density profile for a dark matter halo of $10^{12}\,h^{-1}\,M_{\odot}$ at $z = 1$. The mass density is plotted versus the halocentric distance for SIS (solid line) and NFW halos (dashed line). Lower panel: mass encompassed by radius r.

.

threshold that is certainly well above the smallest mass that we are considering here.

8.3 Effects on the source counts

We can finally estimate the strongly lensed source counts, and compare them with the "unlensed" and weakly lensed counts, in a given wave band, based on the model by Granato et al. (2000). Using the "corrected" magnification distribution $p(A)$ for extended sources, Eq. (59), we compute lensed counts at 850 μm, using SIS and NFW lenses. In Fig. 14, the solid line shows the integral source counts that we expect at 850 μm from the source distribution described in Sect. 6, ignoring lensing. The dot-dashed line includes only weak lensing, using the low-magnification tail of the magnification distribution $p(A,z)$. Since the latter is modeled as a Gaussian with small dispersion around the mean $A = 1$, we can see from Fig. 14 that weak lensing by large-scale structures has very little effect on the integral source counts, even though the variance of the distribution increases with source redshift. The weakly lensed counts are therefore quite similar to the unlensed ones given by Granato et al. (2000). Even the weakly lensed counts, however, fall above the unlensed counts where the number-count function falls most steeply.

The effects of strong lensing from a Sheth & Tormen mass distribution of SIS and NFW lenses is plotted in Fig. 14 as short- and long-dashed lines, respectively; for both density profiles, following the results of section 7, we show in Fig. 14 the results obtained plugging either $A_{\rm E,max} = 10$ (lower lines)or $A_{\rm E,max} = 30$ (upper lines).

We can see that the contribution of strong lensing from a SIS model is here of the order 10^{-2} in the flat part of the counts, while it dramatically raises up in the steepest region, overcoming the weakly lensed counts. This is due to the very strong magnification bias for these sources. First, the source redshift, $z \simeq 5$, is quite high. The probability for a source to undergo a lensing event with high magnification increases with increasing source redshift. Second, and importantly, the steep source counts, discussed in Sect. 6 and by Blain (1996), provide a huge reservoir of source to be magnified above the flux limit of the observation.

At flux densities around 100 mJy, the counts will be dominated by sources magnified by a factor $A \sim 10 - 20$. As we have seen, such quite high magnifications are less probable for the NFW lenses than for the SIS population, which explains the relative values of strongly lensed source counts from NFW and SIS lenses at flux densities $\gtrsim 100$ mJy of Fig. 14. At higher flux densities, lensed sources are depressed by the effect of having taken a maximum amplification $A_{\rm E,max} = 30$.

The substantial magnification bias at flux densities around 100 mJy allows to detect sources otherwise not bright enough for detection. This result may have very interesting consequences on the expected number of SCUBA sources to be found in the whole sky maps produced by the incoming Planck Surveyor Satellite, operating at nine frequency channels between 0.3 and 10 mm (Mandolesi et al. 1998). The detailed study of this issue will be the subject of a forthcoming work (Perrotta et al. 2001).

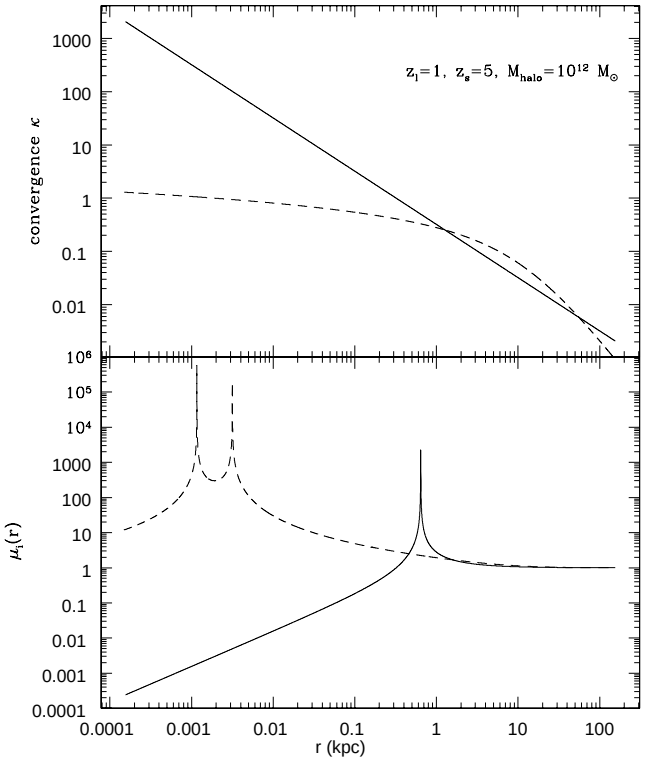

Figure 11. Upper panel: convergence κ as a function of halocentric distance for a halo with $M_{\rm halo} = 10^{12}\,h^{-1}\,M_\odot$ at $z_{\rm l} = 1$. The sources are at $z_{\rm s} = 5$. The plot refers to a SIS (solid line) or a NFW halo (dashed line). Lower panel: Magnification as a function of impact parameter, involving convergence and shear of the gravitational field (see text).

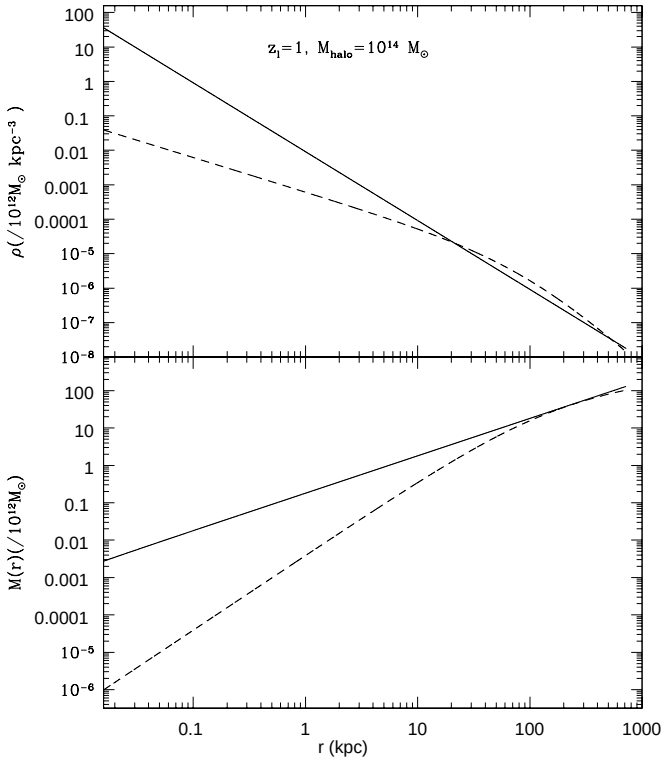

Figure 12. Upper panel: density profile for a dark matter halo of $10^{14}\,h^{-1}\,M_\odot$ at $z = 1$. The mass density is plotted versus the halocentric distance for SIS (solid line) and NFW halos (dashed line). Lower panel: mass encompassed by radius r.

Acknowledgements

We are grateful to L. Danese, L. Moscardini, S. Matarrese, C. Porciani, A. Blain and C. Lacey for useful suggestions and discussions. We remember with gratitude R. De Ritis, and, together with him, we acknowledge E. Piedipalumbo, M. Demianski and A.A. Marino, who kindly provided the coefficients for the approximation of the solution to the Dyer-Roeder equation used in this paper. F.P. wishes to thank the MPA for kind hospitality.

Work supported in part by MURST and ASI.

REFERENCES

Bacon D.J., Refregier A.R., Ellis R.S., 2000, MNRAS 318, 625
Bardeen J.M., Bond J.R., Kaiser N., Szalay A.S., 1986, ApJ 304, 15
Bartelmann M., 1996, A&A 313, 697
Bartelmann M., Huss A., Colberg J.M., Jenkins A., Pearce F.R., 1997, A&A, 330, 1
Bartelmann M., Schneider P., 2001, Phys. Rep. 340, 291
Bhatia V.B., 2000, in proc. IAU Symp. 201 "New Cosmological Data and the Values of the Fundamental Parameter", in press
Binney J., Tremaine S., 1987, *Galactic Dynamics*. (Princeton: Princeton Univ. Press)
Blain A.W., 1996, MNRAS 283, 1340
Blain A. W., Ivison R., Kneib J. P., Smail I., 1999, in: Bunker A.J., van Breugel W.J.M. (eds.), ASP Conf. Ser. *The High-Redshift universe: galaxy formation and evolution at high redshift*, in press, preprint astro-ph/9908024
Blandford R.D., Narayan R., 1992, ARA&A 30, 311
Blandford R.D., Kochanek C.S., 1987, ApJ 321, 658
Blandford R.D., Saust A.B., Brainerd T.G., Villumsen J.V., 1991, MNRAS 251, 600
Bryan G.L., Norman M.L., 1998, ApJ 495, 80
Bunn E. F., White M., 1997, ApJ 480, 6
Carroll S.M., Press W.H., Turner E.L., 1992, ARA&A 30, 499
Clowe D., Luppino G.A., Kaiser N., Gioia I.M., 2000, ApJ 539, 540
Cooray A., 1999, ApJ 512, 83
De Zotti G., Franceschini A., Toffolatti L., Mazzei P., 1996, Ast. Lett. and Comm. 35, 289
Demianski M., De Ritis R., Marino A.A., Piedipalumbo E., 2000, preprint astro-ph/0004376
Dyer C.C., Roeder R.C., 1973, ApJ 180, L31
Ehlers J., Schneider P., 1986, A&A 168, 57
Eke V.R., Cole S., Frenk C.S., 1996, MNRAS 282, 263
Falco E.E., Kochanek C.S., Muñoz J.A., 1998, ApJ 494, 47
Ghigna S., Moore B., Governato F., Lake G., Quinn T., Stadel J., 2000, ApJ, 544, 616
Granato G.L., Silva L., Monaco P., Panuzzo P., Salucci P., De Zotti G., Danese L., 2000, MNRAS, in press
Helbig, P., and the Jvas/Class team, 2000, in proc. IAU Symp. 201 "New Cosmological Data and the Values of the Fundamental Parameter", in press
Huterer D., Cooray, A. R., 1999, AAS 194, 9003
Jain B., Seljak U., 1997, ApJ 484, 560
Jenkins A., Frenk C.S., White S.D.M., Colberg J.M., Cole S., Evrard A.E., Couchman H.M.P., Yoshida N., 2000, MNRAS, submitted, astro-ph/0005260
Kaiser N., 1986, MNRAS 222, 323
Kaiser N., 1992, ApJ 388, 272

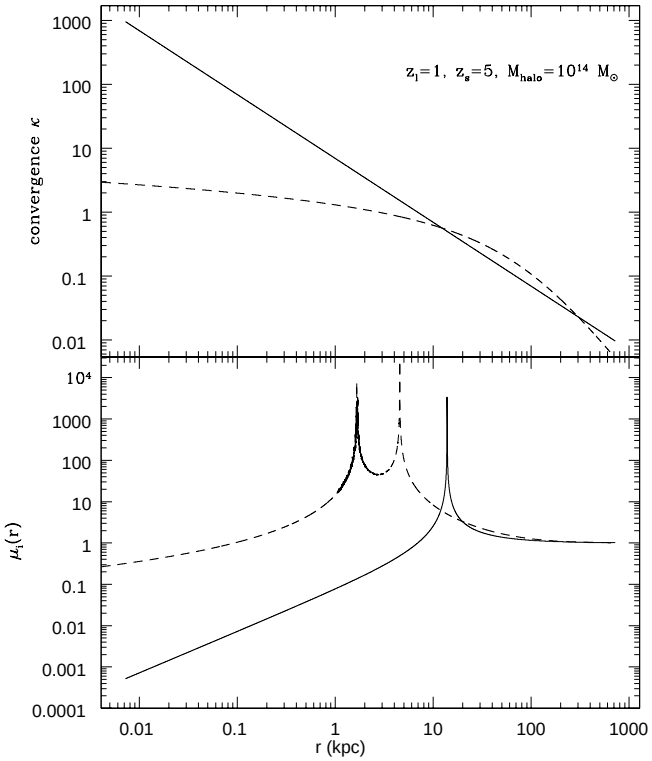

Figure 13. Upper panel: convergence κ as a function of halocentric distance for a halo with $M_{\rm halo} = 10^{14} h^{-1} M_\odot$ at $z_{\rm l} = 1$. The sources are located at $z_{\rm s} = 5$. The plot refers to a SIS (solid line) or a NFW halo (dashed line). Lower panel: magnification as a function of impact parameter, involving convergence and shear of the gravitational field.

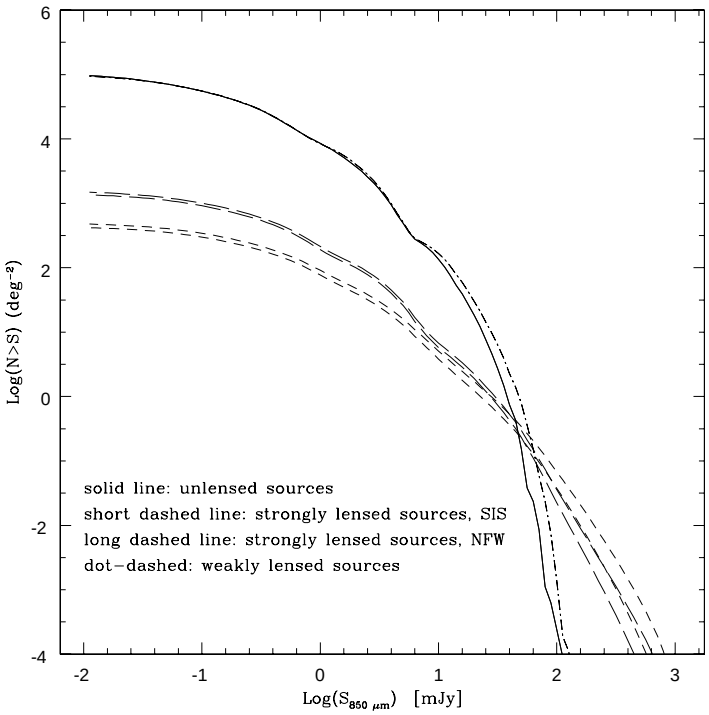

Figure 14. Integral Source counts at 850 μm per square degree. Unlensed counts are given by the solid line, and counts including weak lensing by the dot-dashed line. Short-dashed lines show, for the SIS model, strongly-lensed source counts with $A_{\rm E,max} = 10$ (lower short-dashed lines)or $A_{\rm E,max} = 30$ (upper short-dashed lines), as described in the text. Long-dashed lines are the same for the NFW model of lenses.

Kantowski R., 1998, ApJ 507, 483
Kantowski R., Kao J.K., 2000, preprint astro-ph/0002334
Kent S.M., 1985, ApJ 59, 115
Kitayama T., Suto Y., 1996, ApJ 469, 480
Lacey C., Cole S., 1993, MNRAS 262, 627
Lahav O., Rees M.J., Lilje P.B., Primack J.R., 1991, MNRAS 251, 128
Łokas E.L., Hoffman Y., 2000, astro-ph/0011295
Macias-Perez J.F., Helbig P., Quast R., Wilkinson A., Davies R., 2000, A&A, 353, 419
Mandolesi N. et al., 1998, *Low Frequency Instrument for Planck. A proposal to the European Space Agency*
Mao S.D., Kochanek C.S., 1994, MNRAS 268, 569
Maoz D., Rix H.-W., Gal-Yam A., Gould A., 1997, ApJ 486, 75
Mellier Y., 1999, ARA&A 37, 127
Mihalas D., Binney J., 1981, "Galactic Astronomy", W. H. Freeman and Company, San Francisco, pag. 312
Miralda-Escudé J., 1991, ApJ 380, 1
Monaco P., Salucci P., Danese L., 2000, MNRAS, 311, 279 astro-ph/9907095
Moore B., Quinn T., Governato F., Stadel J., Lake G., 1999, MNRAS, 310, 1147
Nakamura T.T., 1996, Master's Thesis, Univ. Tokyo
Narayan R., 1989, ApJ 339, L53
Narayan R., 1998, NA Rev, 42, 73
Narayan R., Bartelmann M., 1997, in: *Formation of Structure in the Universe*, eds. A. Dekel & J.P. Ostriker (Cambridge University Press)
Navarro J.F., Frenk C.S., White S.D.M., 1997, ApJ 490, 493
Peacock J.A., 1982, MNRAS 199, 987
Peebles P.J.E., 1980, *The Large-Scale Structure of the Universe*, Princeton Univ. Press
Pei Y.C., 1993a, ApJ 403, 7
Pei Y.C., 1993b, ApJ 404, 436
Pei Y.C., 1995, ApJ 440, 485
Perrotta F., Baccigalupi C., Bartelmann M., Danese L., De Zotti G., Granato G. L., 2001, in preparation
Porciani C., Madau P., 2000, ApJ 532, 679
Press W.H., Schechter P., 1974, ApJ 187, 425
Rauch K. P., 1991, ApJ 374, 83
Rix H.-W., Maoz D., Turner E.L., Fukugita M., 1994, ApJ, 435, 49
Saunders W., Rowan-Robinson M., Lawrence A., Efstathiou G., Kaiser N., Ellis R.S., Frenk C.S., 1990, MNRAS 242, 318
Schneider P., 1984 , A&A 140, 119
Schneider P., 1987a, A&A 179, 71
Schneider P., 1987b, A&A 179, 80
Schneider P., 1992, A&A 254, 14
Schneider P., Ehlers J., Falco E.E., 1992, *Gravitational Lenses* (Heidelberg: Springer-Verlag)
Sheth R.K., Tormen G., 1999, MNRAS 308, 119
Sheth R.K., Mo H.J., Tormen G., 1999, preprint astro-ph/9907024
Silva L., Granato G.L., Bressan A., Danese L., 1998, ApJ, 509, 103
Smail I., Ivison R.J., Kneib J.P., Cowie L.L., Blain A.W., Barger A.J., Owen F.N., Morrison G.E., 1999, MNRAS 308, 1061
Turner E.L., Ostriker J.P., Gott J.R. III, 1984, ApJ 284 1
Viana P., Liddle A.R., 1999, MNRAS 303, 535
Vietri M., Ostriker J.P., 1983, ApJ 267, 488
Wallington S., Narayan R., 1993, ApJ 403, 517